Optics Letters

Metasurfaces with high-*Q* resonances governed by topological edge state

Zhidong Gu,[1] Jiaxin Chen,[2] Bofeng Gao,[1] Wei Wu,[1] Zhenyu Zhao,[3] Wei Cai,[1,4] Xinzheng Zhang,[1] Mengxin Ren,[1,*] and Jingjun Xu[1,5]

[1]The Key Laboratory of Weak-Light Nonlinear Photonics, Ministry of Education, School of Physics and TEDA Applied Physics Institute, Nankai University, Tianjin, 300071, China
[2]Science and Technology on Electro-Optical Information Security Control Laboratory, Tianjin, 300308, China
[3]Department of Physics, Shanghai Normal University, Shanghai, 200234, China
[4]e-mail: weicai@nankai.edu.cn
[5]e-mail: jjxu@nankai.edu.cn
*Corresponding author: ren_mengxin@nankai.edu.cn

Received 22 December 2021; revised 23 February 2022; accepted 23 February 2022; posted 23 February 2022; published 30 March 2022

Achieving high-quality (*Q*)-factor resonances in metasurfaces is essential for various applications, including nanolasers, nonlinear optics, and quantum optics. In this work, we propose a high-*Q* metasurface using a topological strategy: constructing the metasurface by stacking two conjugated nanopillar arrays with different topological invariants. Our study shows that a topological edge state steadily appears at the interfaces of the nanopillars, and a sharp transmission resonance with a *Q*-factor of more than 1000 can be obtained. The sensing application of such high-*Q* topological metasurface is also demonstrated, whose figure of merit reaches approximately 145. The proposed strategy and underlying theory can open up new avenues to realize ultrasharp resonances, which can promote numerous potential applications, such as biosensing, optical modulation, and slow-light devices.

https://doi.org/10.1364/OL.451647

Metasurfaces have been regarded as a new platform to realize unique functionalities and novel photonic devices due to their versatile capabilities for controlling light behaviors [1]. The intriguing performances of the metasurfaces largely rely on the occurrence of the optical resonances, which are usually characterized using a parameter called the quality (*Q*)-factor [2]. As the *Q*-factor is proportional to the lifetime of the photons trapped in the nanostructures and also the enhancement of the light–matter interactions, it is typically desirable to maximize the value of the *Q*-factor. The high-*Q*-factor metasurfaces could be used as a cavity for applications that need small mode volumes, large field strength, and flexible tunability, including optical sensing [3,4], electro-optic modulation [5–7], and nonlinear frequency conversion [8–11], among others [12–15]. So far, various methods have been sought after to obtain large *Q*-factor resonances from metasurfaces. For example, ultrasharp Fano-shaped resonance could be achieved through the interference between dark and bright modes at nanoscales [16–19]. In addition, high-*Q*-factor resonances can be observed by transforming the ideal bound states in the continuum (BIC) into the quasi-BIC mode by exploiting structural symmetry breaking or oblique incidence [2,20,21].

Recently, topological photonics has appeared as a favorable framework for harnessing light–matter interactions. The topological photonics combines fundamental concept of topology with resonant nanophotonics [1,22], which provides us with a new way to design photonic local density of states and precisely control the photons at nanoscales [23]. Intriguingly, if one combines two optical systems with different topological properties to form a heterostructure, a robust edge state with tightly localized field will appear at the interface region. A famous example could be the Su–Schrieffer–Heeger (SSH) state in a one-dimensional system when the Zak phase of the occupied band on one side of the chain is different from that on the other side [24,25]. A major advantage of the topological states is their robustness, namely, such states are well immune to the possible perturbations in the sizes of the nanostructures introduced during the practical fabrication process [25,26]. A number of interesting phenomena and functionalities have been demonstrated based on constructing topological photonic states, for example, unidirectional propagation [27,28], boosted thermo-optical switching [29], topological edge-mode lasing [30,31], strengthened optical harmonic generation [26,32], enhanced circular dichroism [33], and negative refraction of waves [34].

In this paper, we use a topological strategy to construct a high-*Q*-factor metasurface. By stacking together two conjugated laminar nanopillar (NP) arrays with different topological invariants, a topological edge state steadily appears at the interface and an ultrasharp transmission resonance can be obtained in the visible spectral range. The linewidth and corresponding *Q*-factor can reach 0.7 nm and 1045, respectively. The optical responses of the metasurfaces could be easily altered by the geometric parameters, such as the radii and the layer numbers of the NPs. Furthermore, its application for refractive index sensing is demonstrated, whose figure of merit (FOM) can reach approximately 145. Such high *Q*-factor resonances underlying the topological edge state may provide a potential basis for many

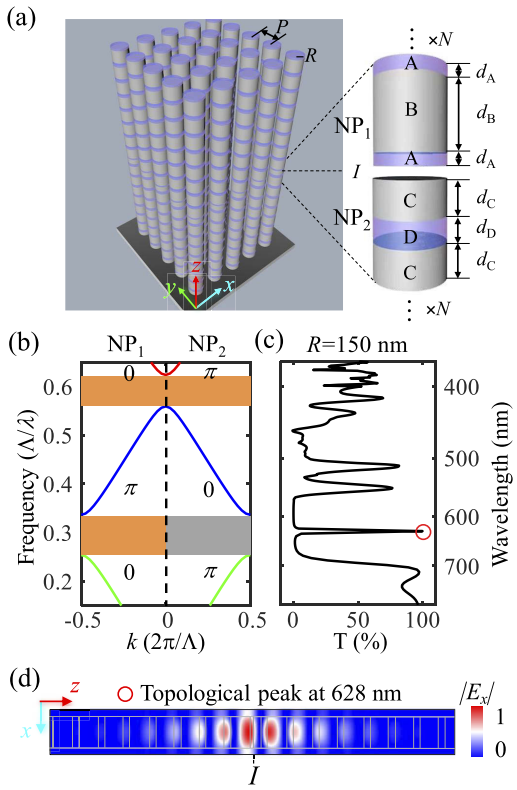

Fig. 1. Design of topological metasurface. (a) Schematic of the metasurface composed of an NP array on a fused-quartz substrate. The lattice constant of the metasurface and radius of the NP are denoted as P and R, respectively. Each NP is constructed by stacking two laminar structures (labeled here as NP_1 and NP_2), which forms an interface at I. Details of the unit cells of the NP_1 and NP_2 are given on the right. Layers A, D are TiO_2 with thickness $d_D = 2d_A = 60$ nm, and layers B, C are SiO_2 with thickness $d_B = 2d_C = 170$ nm. The two unit cells have an identical structure, except their origins are respectively defined in the center of the SiO_2 layer or TiO_2 layer. (b) Calculated band structures of NP_1 (left) and NP_2 (right) with infinite layers. The Zak phase of each band is indicated by numbers (0 or π). Gray and orange rectangles present bandgaps with positive and negative signs of topological invariants, respectively. A topological edge state (TES) would exist in the lowest gap (at a frequency of approximately 0.3), where the signs of the topological invariants are opposite in the two NPs. (c) Transmission spectrum of the metasurface with $R = 150$ nm and N under normal incidence, where the sharp TES is marked by a red circle. (d) Calculated electric field distributions corresponding to the TES at 628 nm.

potential applications, for instance, exciton–polariton condensates, nanolasers, optical sensors, nonlinear photonic devices, and so on.

Figure 1(a) depicts the structure of the topological metasurface, which consists of a square-lattice NP array with a lattice constant P of 400 nm on a fused quartz substrate. Each NP is formed by stacking two laminar structures (labeled here as NP_1 and NP_2, whose unit cells are given on the right). Each NP contains N unit cells, and the interface between the NPs is labeled by I. Layers A and D in purple are titanium dioxide (TiO_2), while layers B and C in gray are silicon dioxide (SiO_2). Their thicknesses are chosen as $d_B = 2d_C = 170$ nm and $d_D = 2d_A = 60$ nm, thus the sizes of the unit cells of the two NPs are identical, i.e., $\Lambda = 2d_A + d_B = 2d_C + d_D = 230$ nm. The optical properties of the metasurface are studied using a finite-element method (Comsol Multiphysics), in which the refractive indices of TiO_2 and SiO_2 are set as 2.34 and 1.45, respectively. The metasurface is excited by a normally incident x-polarized plane wave. To reveal the topological feature of the NPs, we calculate the band structures of the two NPs in a normalized frequency Λ/λ range from 0.15 to 0.65, as shown in Fig. 1(b). The band structures of the NP_1 and NP_2 are the same because the two NPs essentially have the same geometries. However, because the origins of the unit cells are defined at the different inversion centers of the NP structures (i.e., center of the SiO_2 layer for NP_1 and that of the TiO_2 layer for NP_2), they would have different topological features. The topological properties of the NPs are described by the Zak phase, and that of the nth band can be calculated via [25]

$$\theta_n^{\mathrm{Zak}} = \int_{-\frac{\pi}{\Lambda}}^{\frac{\pi}{\Lambda}} [i \int_{\mathrm{unitcell}} \varepsilon(z)\mu_{n,k}^*(z)\delta k \mu_{n,k}(z)]dk, \quad (1)$$

where $\varepsilon(z)$ describes the distribution of permittivity in the NP structures and $\mu_{n,k}(z)$ represents the eigenfunction of the electric field at the nth photonic passband with a Bloch wave vector of k. The Zak phase of each passband is labeled in Fig. 1(b), which are 0, π, 0 for NP_1, and π, 0, π for NP_2. A topological invariant could be further defined for nth bandgap by summing the Zak phase of all the passbands below it:

$$\mathrm{sgn}[\zeta^{(n)}] = (-1)^n \exp(i \sum_{m=0}^{n-1} \theta_m^{\mathrm{Zak}}). \quad (2)$$

It can be found that the signs of the invariants in the two NPs are opposite for the bandgaps around the frequency Λ/λ of 0.3, where a topological edge state (TES) would occur at the interface I according to the SSH model [24,25]. To intuitively reveal the existence of the TES, we further simulate the transmission spectrum for the metasurface with $N = 8$ and $R = 150$ nm, as shown in Fig. 1(c). A sharp transmission peak corresponding to the TES appears around 628 nm (marked by a circle), which exactly locates in the topological bandgap. Figure 1(d) illustrates the electric field (E_x) distribution in the xoz-plane at the TES wavelength. It is clear that the electric field is tightly localized near the interface I, and the field amplitude decreases for the positions away from the interface. This implies a resonance mode with high-Q-factor, which is approximately 114 calculated by the ratio between the center wavelength and the full width at half maximum (FWHM) of the TES transmission resonance in Fig. 1(c).

The dependence of transmission spectra on the radii of NPs are shown in Fig. 2(a). As the radii increase, resonances show a redshift and the bandwidths of the resonances become narrower gradually [35]. In addition, we calculate the Q-factors as a function of the radius R, as shown in Fig. 2(b). As R gradually increases to 200 nm, the Q-factor grows rapidly up to 1045. It is obvious that there is bare energy localized in the NP structures when $R = 50$ nm. In contrast, the strong electric fields localize near the interface, which result in the narrow linewidth and high-Q-factor when $R = 200$ nm.

The influence of the number of unit cells N contained in the NPs on the transmission spectra of the TES is shown in Fig. 3. Notably, the central wavelengths of TESs are kept nearly constant, and only the linewidths of resonances become narrower when the N increases. As the N approaches infinity, the Q-factor would approach infinity. However, considering the resolution

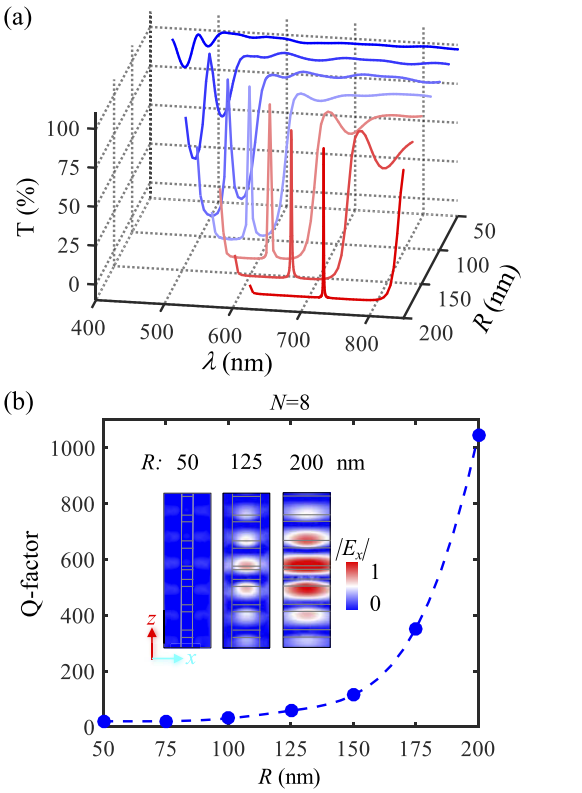

Fig. 2. Transmission spectra and Q-factors as a function of NP radius R. (a) Transmission spectra of metasurfaces with different radii, R = 50, 75, 100, 120, 150, 175, and 200 nm, whereas N is fixed as 8. The resonances experience a redshift and become narrower as R increases. (b) Q-factors of the TES for different radii R, which could achieve 1045 when R = 200 nm. Insets show the representative electric field distributions of TESs for R of 50, 125, and 200 nm.

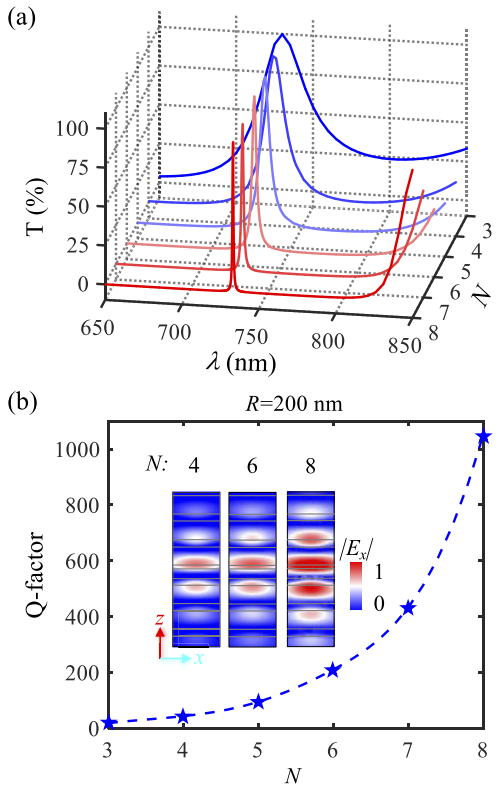

Fig. 3. Transmission spectra and Q-factors as a function of number of unit cells N contained in each NP. (a) TES resonances become sharper when N increases from 3 to 8; however, the central wavelength positions remain nearly unchanged. The R is fixed as 200 nm in these cases. (b) Dependence of Q-factor on the N, which increases rapidly as N increases. Insets give the representative electric field distributions of TESs for N of 4, 6, and 8.

of practical spectrometers, we here only show the results for N between 3 and 8, although the measured Q-factors could be less than the simulated ones because of the fabrication imperfection (such as tilted sidewalls, material losses, etc.) in realistic devices. The inserted pictures describe the field distributions of the TES when the N is 4, 6, and 8, respectively.

Benefiting from the high-Q-factor and tight field localization of the TES resonance, we can expect that the proposed topological NP metasurfaces can be used for sensing applications. The sensing principle is based on the spectral resonance shift of the metasurface caused by the changes of the ambient refractive index. Figure 4(a) illustrates a schematic of the operation of the refractive index sensor based on our metasurface. When the liquid droplets are dropped on the metasurface array and immerse into the NP arrays due to the capillary force, the refractive index between the NPs can be efficiently altered. The metasurface with R = 200 nm and N = 8 is chosen here to construct the sensor. As shown in Fig. 4(b), the resonant peaks shift from 729 to 827 nm as the liquid refractive indices increase from 1.0 to 2.0. It is clear from Fig. 4(c) that the wavelength shift ($\Delta\lambda$) appears to be linearly dependent on the refractive index change Δn. Through linear fitting, the sensing sensitivity $\Delta\lambda/\Delta n$ of the topological metasurface is determined as 100 nm per refractive index unit (RIU). By further considering the linewidth of the resonance, the figure of merit (FOM), an important parameter to evaluate

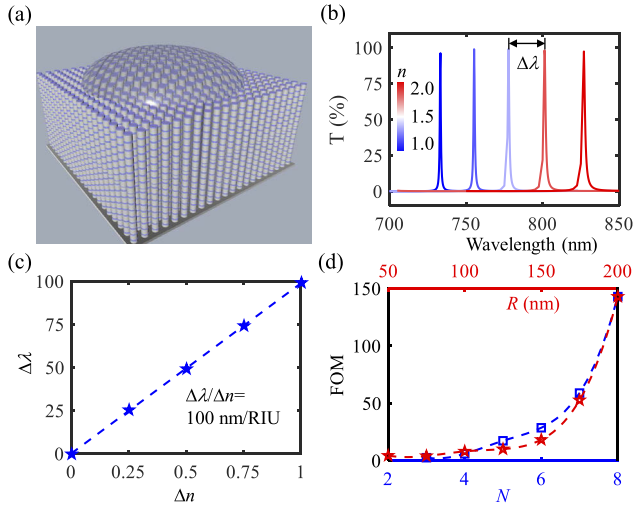

Fig. 4. Performance of a refractive index sensor based on our topological metasurface. (a) Sketch of the refractive index sensor. Liquid is dropped onto the metasurface array, resulting in efficient changes of the refractive index between the NPs. (b) Spectral shift induced by ambient refractive index increase from 1.0 to 2.0. (c) Wavelength shift $\Delta\lambda$ against refractive index changes Δn. The sensing sensitivity ($\Delta\lambda/\Delta n$) can be determined by linear fitting of the curve. (d) Dependence of FOM on R (pentagram) and N (empty square). The FOM can be efficiently improved by either increasing R or N.

the performances of sensors, can be defined by the ratio between the sensing sensitivity to the FWHM of the resonance. As indicated in Figs. 2 and 3, the FWHM would decrease dramatically as R and N increase, thus leading to an improved FOM for larger R and N. As shown in Fig. 4(d), keeping N as 8 and increasing R from 50 nm to 200 nm would induce a significant increase of FOM (solid star dots). Similarly, when N increases from 3 to 8 with R fixed at 200 nm, the FOM also dramatically increases, and reaches approximately 145. This value is larger than the reported sensor based on the silicon nanocylinder metasurfaces with the FOM of 5.4 [36,37], the sensor by the electromagnetically induced transparency (EIT) dielectric metasurfaces with the FOM of 103 [16], and the quasi-BIC design (FOM=80.6) [38].

In summary, we have proposed a topological strategy to obtain high-Q resonances in metasurfaces. By piling up two conjugated laminar NP arrays with different topological invariants, the TES would appear at the interface, resulting in an ultrasharp resonance in transmission spectrum. The optical properties of the metasurfaces can be easily altered by the geometric parameters, such as the radii R and the layer numbers N of the NPs. A Q-factor of 1045 is achieved for $R = 200$ nm and $N = 8$. Furthermore, we demonstrate its application for refractive index sensing, whose FOM can reach approximately 145. Our results pave a new way toward engineering of sharp resonances in metasurfaces for applications of lasing, sensing, and nonlinear photonics.

Funding. National Key Research and Development Program of China (2017YFA0303800, 2017YFA0305100, 2019YFA0705000); National Natural Science Foundation of China (11774185, 11904182, 12074200, 12174202, 61775106, 91750204, 92050114); Guangdong Major Project of Basic and Applied Basic Research (2020B0301030009); 111 Project (B07013); Program for Changjiang Scholars and Innovative Research Team (PCSIRT) (IRT0149); Fundamental Research Funds for the Central Universities (010-63201003, 010-63201008, 010-63201009, 010-63211001); Tianjin Youth Talent Support Program.

Disclosures. The authors declare no conflicts of interest.

Data availability. Data underlying the results presented in this paper are not publicly available at this time but may be obtained from the authors upon reasonable request.

REFERENCES

1. A. I. Kuznetsov, A. E. Miroshnichenko, M. L. Brongersma, Y. S. Kivshar, and B. Luk'yanchuk, Science **354**, aag2472 (2016).
2. K. Koshelev, S. Lepeshov, M. Liu, A. Bogdanov, and Y. Kivshar, Phys. Rev. Lett. **121**, 193903 (2018).
3. O. Yavas, M. Svedendahl, P. Dobosz, V. Sanz, and R. Quidant, Nano Lett. **17**, 4421 (2017).
4. J. Wang, J. Kühne, T. Karamanos, C. Rockstuhl, S. A. Maier, and A. Tittl, Adv. Funct. Mater. **31**, 2104652 (2021).
5. H. Weigand, V. V. Vogler-Neuling, M. R. Escalé, D. Pohl, F. U. Richter, A. Karvounis, F. Timpu, and R. Grange, ACS Photonics **8**, 3004 (2021).
6. I.-C. Benea-Chelmus, S. Mason, M. L. Meretska, D. L. Elder, D. Kazakov, A. Shams-Ansari, L. R. Dalton, and F. Capasso, arXiv:2108.03539 (2021).
7. B. Gao, M. Ren, W. Wu, W. Cai, and J. Xu, Sci. China: Phys., Mech. Astron. **64**, 240362 (2021).
8. A. P. Anthur, H. Zhang, R. Paniagua-Dominguez, D. A. Kalashnikov, S. T. Ha, T. W. Maß, A. I. Kuznetsov, and L. Krivitsky, Nano Lett. **20**, 8745 (2020).
9. L. Carletti, S. S. Kruk, A. A. Bogdanov, C. De Angelis, and Y. Kivshar, Phys. Rev. Res. **1**, 023016 (2019).
10. L. Carletti, K. Koshelev, C. De Angelis, and Y. Kivshar, Phys. Rev. Lett. **121**, 033903 (2018).
11. J. Ma, F. Xie, W. Chen, J. Chen, W. Wu, W. Liu, Y. Chen, W. Cai, M. Ren, and J. Xu, Laser Photonics Rev. **15**, 2000521 (2021).
12. D. Bouchet, M. Mivelle, J. Proust, B. Gallas, I. Ozerov, M. F. Garcia-Parajo, A. Gulinatti, I. Rech, Y. De Wilde, N. Bonod, K. Valentina, and B. Sébastien, Phys. Rev. Appl. **6**, 064016 (2016).
13. T. Feng, Y. Xu, Z. Liang, and W. Zhang, Opt. Lett. **41**, 5011 (2016).
14. W. Zhao, X. Leng, and Y. Jiang, Opt. Express **23**, 6858 (2015).
15. A. Utyushev, I. Isaev, V. Gerasimov, A. Ershov, V. Zakomirnyi, I. Rasskazov, S. Polyutov, H. Ågren, and S. Karpov, Opt. Express **28**, 1426 (2020).
16. Y. Yang, I. I. Kravchenko, D. P. Briggs, and J. Valentine, Nat. Commun. **5**, 5753 (2014).
17. S. Campione, S. Liu, L. I. Basilio, L. K. Warne, W. L. Langston, T. S. Luk, J. R. Wendt, J. L. Reno, G. A. Keeler, and I. Brener, ACS Photonics **3**, 2362 (2016).
18. M. F. Limonov, M. V. Rybin, A. N. Poddubny, and Y. S. Kivshar, Nat. Photonics **11**, 543 (2017).
19. E. Melik-Gaykazyan, K. Koshelev, J.-H. Choi, S. S. Kruk, A. Bogdanov, H.-G. Park, and Y. Kivshar, Nano Lett. **21**, 1765 (2021).
20. C. W. Hsu, B. Zhen, A. D. Stone, J. D. Joannopoulos, and M. Soljačić, Nat. Rev. Mater. **1**, 16048 (2016).
21. M. Rybin and Y. Kivshar, Nature **541**, 164 (2017).
22. M. A. Gorlach, X. Ni, D. A. Smirnova, D. Korobkin, D. Zhirihin, A. P. Slobozhanyuk, P. A. Belov, A. Alù, and A. B. Khanikaev, Nat. Commun. **9**, 909 (2018).
23. M. S. Rider, S. J. Palmer, S. R. Pocock, X. Xiao, P. Arroyo Huidobro, and V. Giannini, J. Appl. Phys. **125**, 120901 (2019).
24. W. Su, J. Schrieffer, and A. J. Heeger, Phys. Rev. Lett. **42**, 1698 (1979).
25. M. Xiao, Z. Zhang, and C. T. Chan, Phys. Rev. X **4**, 021017 (2014).
26. D. Smirnova, S. Kruk, D. Leykam, E. Melik-Gaykazyan, D.-Y. Choi, and Y. Kivshar, Phys. Rev. Lett. **123**, 103901 (2019).
27. Z. Wang, Y. Chong, J. D. Joannopoulos, and M. Soljačić, Nature **461**, 772 (2009).
28. M. Wang, R.-Y. Zhang, L. Zhang, D. Wang, Q. Guo, Z.-Q. Zhang, and C. T. Chan, Phys. Rev. Lett. **126**, 067401 (2021).
29. C. Li, X. Hu, W. Gao, Y. Ao, S. Chu, H. Yang, and Q. Gong, Adv. Opt. Mater. **6**, 1701071 (2018).
30. P. St-Jean, V. Goblot, E. Galopin, A. Lemaître, T. Ozawa, L. Le Gratiet, I. Sagnes, J. Bloch, and A. Amo, Nat. Photonics **11**, 651 (2017).
31. H. Zhao, P. Miao, M. H. Teimourpour, S. Malzard, R. El-Ganainy, H. Schomerus, and L. Feng, Nat. Commun. **9**, 981 (2018).
32. S. S. Kruk, W. Gao, D.-Y. Choi, T. Zentgraf, S. Zhang, and Y. Kivshar, Nano Lett. **21**, 4592 (2021).
33. J. Chen, L. Wang, W. Wu, W. Cai, H. Liu, M. Ren, and J. Xu, Phys. Rev. Appl. **16**, L031001 (2021).
34. H. Chu, Z.-G. Chen, Y. Lai, and G. Ma, Phys. Rev. Appl. **16**, 044006 (2021).
35. P. Fan, Z. Yu, S. Fan, and M. L. Brongersma, Nat. Mater. **13**, 471 (2014).
36. O. Yavas, M. Svedendahl, and R. Quidant, ACS Nano **13**, 4582 (2019).
37. M. L. Tseng, Y. Jahani, A. Leitis, and H. Altug, ACS Photonics **8**, 47 (2021).
38. Y. Chen, C. Zhao, Y. Zhang, and C. Qiu, Nano Lett. **20**, 8696 (2020).